Analysis of capillary pressure effect on the seismic response of a CO_2-storage site applying multiphase flow and wave propagation simulators

Lucas A. Macias [a,*], Gabriela B. Savioli [a], Juan E. Santos [b,c,d], José M. Carcione [e], Davide Gei [e]

[a] Laboratorio de Ingeniería de Reservorios, Instituto del Gas y del Petróleo, Facultad de Ingeniería, Universidad de Buenos Aires, Av. Las Heras 2214 Piso 3, C1127AAR Buenos Aires, Argentina
[b] Instituto del Gas y del Petróleo, Facultad de Ingeniería, Universidad de Buenos Aires, CONICET, Argentina
[c] Universidad de La Plata, Argentina
[d] Department of Mathematics, Purdue University, 150 N. University Street, West Lafayette, IN 47907-2067, USA
[e] Istituto Nazionale di Oceanografia e di Geofisica Sperimentale (OGS), Borgo Grotta Gigante 42c, 34010 Sgonico, Trieste, Italy

ARTICLE INFO

ABSTRACT

We analyze the influence of capillary pressure on the seismic response of a saline aquifer, where CO_2 has been stored in the Utsira Sand at the Sleipner field. For this purpose, we present a novel methodology integrating numerical simulation of CO_2–brine flow and seismic wave propagation, using a geological model that includes mudstone layers and natural apertures. The simultaneous flow of CO_2 and brine in an aquifer is modeled by the differential equations that describe the two-phase fluid flow in porous media. The multiphase flow functions are determined from well-log data, using the relation between resistivity index, relative permeabilities and capillary pressure. Seismic monitoring is performed with a wave equation that includes attenuation and dispersion effects due to mesoscopic scale heterogeneities in the petrophysical and fluid properties. The fluid simulator properly models the CO_2 injection and upward migration, obtaining accumulations below the mudstone layers as injection proceeds. Moreover, we are able to identify the time-lapse distribution of CO_2 from the synthetic seismograms, which show the typical pushdown effect due to the spatial distribution of CO_2. Finally, a sensitivity analysis is performed by modifying the capillary pressure threshold in order to evaluate its effect over the CO_2 plume and the corresponding synthetic seismogram.

© 2015 Elsevier Ltd. All rights reserved.

1. Introduction

The first industrial CO_2 injection project began in 1996 at the Sleipner gas field in Norway (Baklid et al., 1996). In this project, CO_2 separated from natural gas is being injected in the Utsira Sand, a high permeable sandstone, with several mudstone layers that limit the vertical migration of the CO_2 (Arts et al., 2008; Chadwick et al., 2005). Numerical modeling of CO_2 injection and storage is an important tool to analyze the effectiveness of this procedure in reducing the amount of greenhouse gases in the atmosphere (Arts et al., 2008).

We introduce a methodology to simulate the CO_2 injection and storage in saline aquifers, combined with a petrophysical model of the Utsira Sand in order to compare our results against actual data obtained from an undergoing CO_2 storage project. The petrophysical model is based on initial porosity and clay content and considers the variation of rock properties with pore pressure and saturation (Carcione et al., 2003). Therefore, these properties are time dependent due to the CO_2 injection, but they change at a much slower rate than pressure and saturations. As a consequence, we have two time scales, and we use a larger time step to update petrophysical properties than to run the flow simulator. The time increment for updating was chosen empirically, as the maximum time step at which the saturation distributions remain unchanged (30 days).

The initial porosity is assumed to have a fractal spatial distribution (Frankel and Clayton, 1986) and the permeability is assumed to be anisotropic, obtained from first principles as a function of porosity and grain sizes.

Several authors have conducted extensive analysis in order to determine the topographic, stratigraphic and petrophysical characterizations of the Utsira Sand based on well-log, 2D and 3D-seismic data, as well as time-lapse seismic imaging of the CO_2 plume (Chadwick et al., 2004, 2009; Zweigel et al., 2004). Our model for the Utsira Sand takes into account these findings, which makes it closer to the actual properties.

This geological model can simulate embedded mudstone layers of very low permeability. Brine and CO_2 relative permeabilities and capillary pressure are determined from well-log data, using the relation between resistivity index, relative permeabilities and capillary pressure (Li, 2011).

The Black-Oil formulation for two-phase flow in porous media (Aziz and Settari, 1985) is used to simulate the CO_2–brine flow. The numerical solution is obtained with the public-domain software BOAST (Fanchi, 1997), which solves the differential equations by finite differences with the IMPES algorithm (IMplicit Pressure Explicit Saturation) (Aziz and Settari, 1985). The basic idea of IMPES is to obtain a single pressure equation combining the flow equations. Once pressure is implicitly computed for the new time, saturation is then updated explicitly. After applying the fluid flow model to obtain the distribution for CO_2 saturation and pressure within the saline aquifer, we use this information as an input to our own wave propagation simulator in order to obtain the corresponding synthetic seismograms.

The wave propagation is based on an isotropic viscoelastic model that considers dispersion and attenuation effects. The complex P- and S-wave moduli are determined using the Zener model to represent the viscoelastic behavior of the material in the brine saturated mudstone layers (Carcione, 2014). Outside the mudstone layers, we use White's theory (White et al., 1975) to model P-wave attenuation based on a model of porous layers alternately saturated with brine and CO_2. S-wave attenuation is also taken into account by making the shear modulus complex and frequency dependent using another relaxation mechanism related to the P-wave attenuation model (Carcione et al., 2012).

Summarizing, in this paper we present a new approach that combines fluid flow and wave propagation simulation for CO_2 storage inside a saline aquifer. The results of the flow simulator applied to the petrophysical (poro-viscoelastic) model, allows us to calculate the phase velocities and attenuation coefficients of the P- and S-waves. The wave propagation model needs these velocities and coefficients to obtain the corresponding seismic images.

Also, we use this approach to evaluate the effect of the capillary pressure on the propagation of the CO_2 plume and its corresponding synthetic seismograms.

2. Model description

In this work we present a new approach that consists in a chained set of models that produce the storage site seismic images that approximate the real ones, based on real data. First, we obtain the distribution of CO_2 and brine saturations and pressures in an aquifer by applying a fluid flow simulator. Then, we feed that information to the petrophysical model which yields updated porosity, permeabilities, dry-rock bulk and shear moduli and computed values of velocity and attenuation of wave propagation in this media. Finally, we take those parameters and run our own wave propagation simulator to obtain the seismic response.

2.1. CO_2 injection model

Our first step is to model the simultaneous flow of CO_2 and brine in an aquifer. This is achieved by solving the differential equations that describe the two-phase fluid flow in porous media (Aziz and Settari, 1985). These equations, obtained by combining the mass conservation equations with Darcy's empirical law, are

$$\nabla \cdot \left(\underline{\kappa} \left(\frac{k_{rg}}{B_g \eta_g}(\nabla p_g - \rho_g g \nabla z) + \frac{R_s k_{rb}}{B_b \eta_b}(\nabla p_b - \rho_b g \nabla z) \right) \right)$$

$$+ \frac{q_g}{\rho_g^{SC}} = \frac{\partial \left[\phi \left(\frac{S_g}{B_g} + \frac{R_s S_b}{B_b} \right) \right]}{\partial t}, \tag{1}$$

$$\nabla \cdot \left(\underline{\kappa} \frac{k_{rb}}{B_b \eta_b}(\nabla p_b - \rho_b g \nabla z) \right) + \frac{q_b}{\rho_b^{SC}} = \frac{\partial \left[\phi \frac{S_b}{B_b} \right]}{\partial t}, \tag{2}$$

where g, b denote CO_2 and brine phases, respectively and the unknowns are the fluid pressures p_β and saturations S_β ($\beta = b, g$). Also ρ_β is the density, ρ_β^{SC} is the density at standard conditions, q_β the injection mass rate per unit volume, $k_{r\beta}$ the relative permeability, η_β the viscosity, ϕ the porosity, $\underline{\kappa}$ the absolute permeability tensor, g the gravity constant and z the depth. Finally, R_s, B_g and B_b are the PVT parameters, which are the CO_2 solubility in brine, CO_2 formation volume factor and brine formation factor respectively.

These equations were obtained assuming that the CO_2 component may dissolve in the brine phase, but the brine is not allowed to vaporize into the CO_2 phase.

Two algebraic equations relating the saturations and pressures complete the system:

$$S_b + S_g = 1, \qquad p_g - p_b = P_C(S_b), \tag{3}$$

where $P_C(S_b)$ is the capillary pressure function.

Appendix A describes how these differential equations are obtained and solved.

2.1.1. Multiphase flow functions

Two types of multiphase flow functions appear on the system of equations (Eqs. (1)–(3)): relative permeability and capillary pressure, where both are function of saturation. In order to obtain these parameters for CO_2 and brine, we compute the resistivity index from actual well-log data and then apply a procedure that correlates all three variables (Li, 2011).

The resistivity index ($RI(S_b)$) is computed from the conductivity measurements as

$$RI(S_b) = \frac{\sigma(1)}{\sigma(S_b)}, \tag{4}$$

where $\sigma(1)$ is the conductivity at full brine saturated rock obtained from well-log data and $\sigma(S_b)$ is the conductivity at saturation S_b, which is determined as follows: (Picotti et al., 2012):

$$\sigma(S_b) = (1 - \phi)\sigma_q^\gamma + \phi(1 - S_b)\sigma_g^\gamma + \phi S_b \sigma_b^\gamma, \tag{5}$$

where σ_b, σ_g and σ_q are the brine, CO_2 and grain conductivities, respectively. Moreover, γ is a free parameter assumed equal to 0.5 according to the CRIM model (Carcione et al., 2007).

Once the resistivity index is calculated, the relative permeability curves can be obtained as functions of brine saturations as

$$k_{rb}(S_b) = \frac{\Lambda(S_b)}{RI(S_b)}, \tag{6}$$

$$k_{rg}(S_b) = (1 - \Lambda(S_b))^2[1 - \kappa_{rb}(S_b)], \tag{7}$$

with

$$\Lambda(S_b) = \frac{S_b - S_{rb}}{1 - S_{rb}}, \tag{8}$$

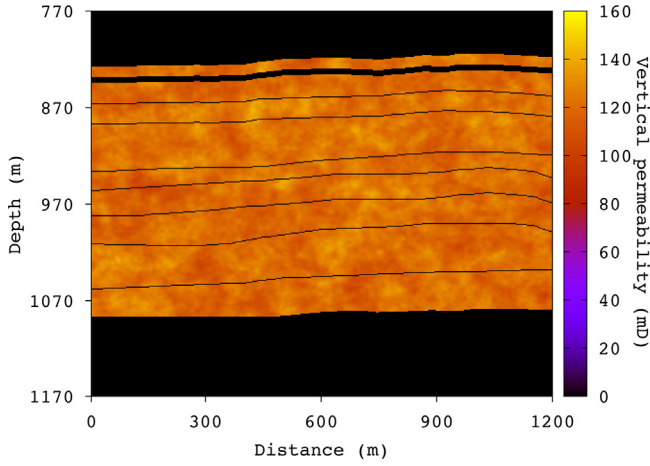being S_{rb} the residual brine saturation.

Fig. 1. Initial vertical permeability map.

To obtain the capillary pressure function ($P_c(S_b)$) it is necessary to adjust the brine relative permeability curve with a free parameter n,

$$\kappa_{rb}(S_b) = \frac{\Lambda(S_b)}{RI(S_b)} = \Lambda(S_b)^{((2+n)/n)}. \tag{9}$$

Then, $P_c(S_b)$ can be represented using a potential model as follows:

$$P_{cD}(S_b) = \Lambda(S_b)^{(-1/n)}, \tag{10}$$

with

$$P_{cD}(S_b) = \frac{P_c(S_b)}{P_{ce}}, \tag{11}$$

where P_{cD} is the dimensionless capillary pressure and P_{ce} is the entry or threshold pressure, that is to say, the pressure at which the CO_2 phase is sufficiently connected to allow flow. This parameter was used to perform the capillary pressure sensitivity analysis presented in this work.

2.2. Petrophysical model

This section describes the procedure used to determine the petrophysical and fluid flow parameters needed in the CO_2 injection and seismic simulations. Firstly, it is used to calculate the aquifer properties update during CO_2 injection. Secondly, it allows us to calculate the phase velocities and quality factors for the P- and S-waves, which are necessary to run the wave propagation simulation.

The porosity pressure dependence is based on the following relationship between porosity and average pore pressure $p(t) = S_b p_b(t) + S_g p_g(t)$,

$$\frac{(1 - \phi_c)}{K_{solid}}(p(t) - p_H) = \phi_0 - \phi(t) + \phi_c \ln \frac{\phi(t)}{\phi_0}, \tag{12}$$

where ϕ_c is a critical porosity, ϕ_0 is the initial porosity at hydrostatic pore pressure p_H and K_{solid} is the bulk modulus of the solid grains composing the dry porous matrix (Carcione et al., 2003). The rock is assumed to have two components: quartz (bulk modulus of 40 GPa) and clay (bulk modulus of 15 GPa). K_{solid} is computed as
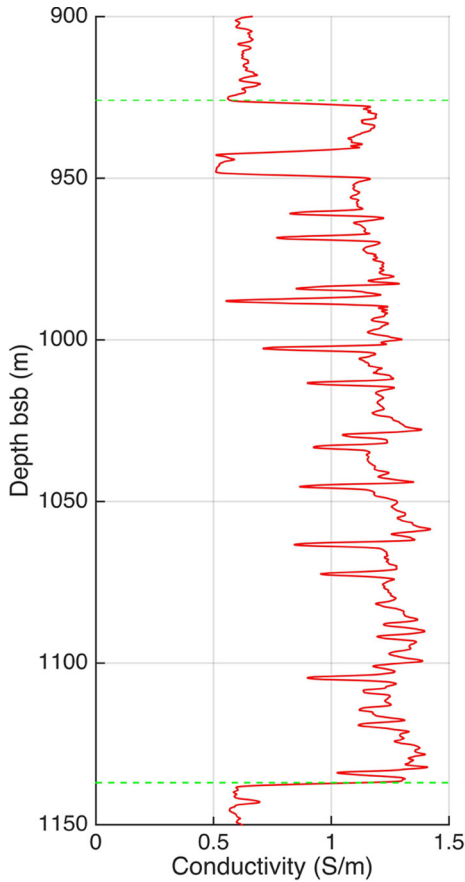
(a) Conductivity log
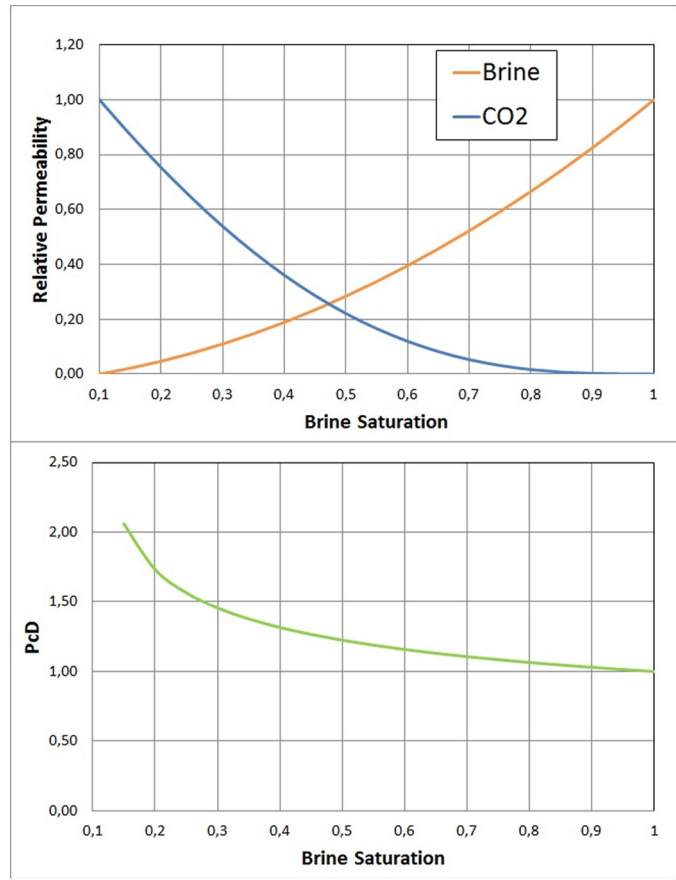
(b) Multiphase fow functions

Fig. 2. Relative permeabilities and dimensionless capillary pressure from Utsira conductivity log (well 15/9-13).
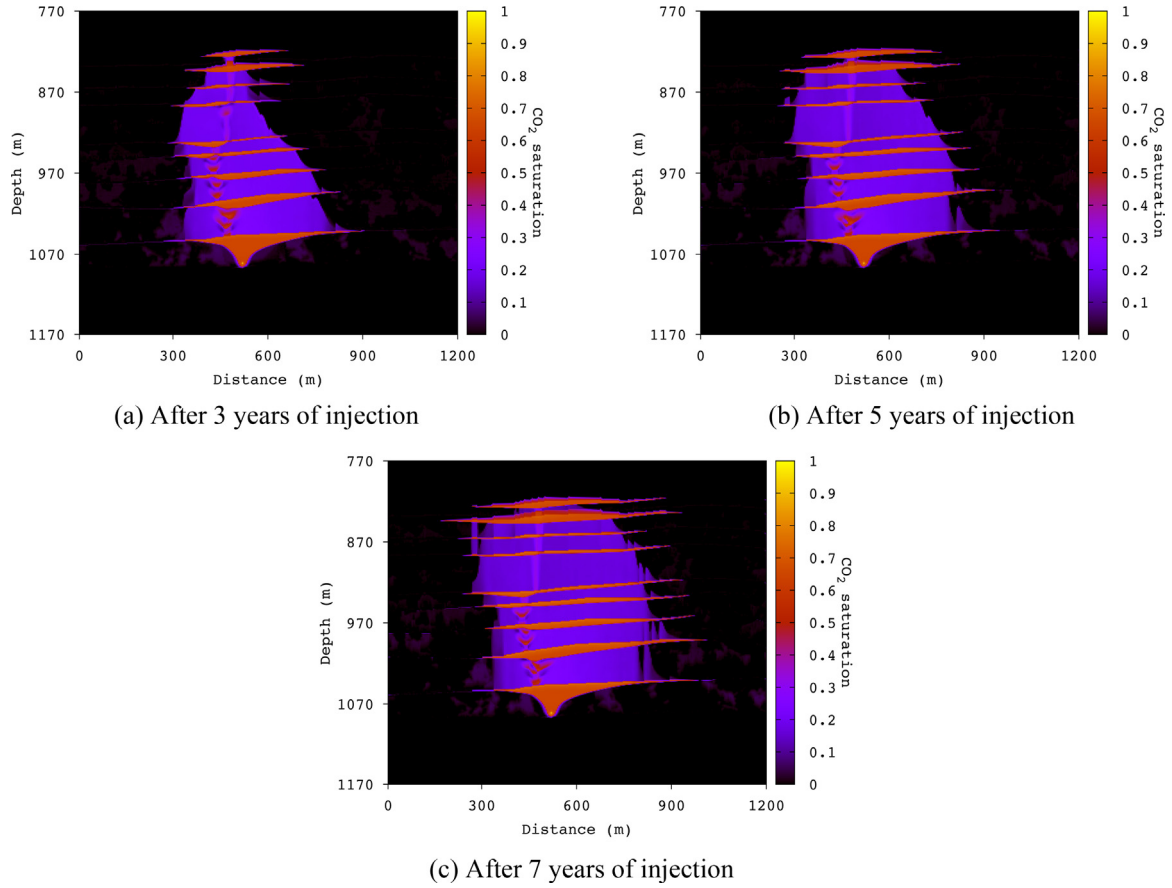
(a) After 3 years of injection

(b) After 5 years of injection

(c) After 7 years of injection

Fig. 3. CO_2 saturation maps.

the arithmetic average of the Hashin Shtrikman upper and lower bounds.

The relationship among horizontal permeability κ_x, porosity and clay content C is Carcione et al. (2003),

$$\frac{1}{\kappa_x(t)} = \frac{45(1-\phi(t))^2}{\phi(t)^3} \left(\frac{(1-C)^2}{R_q^2} + \frac{C^2}{R_c^2} \right), \tag{13}$$

where R_q and R_c are the average radii of the sand and clay grains. As absolute permeability is anisotropic, we assume the following relationship between the horizontal and vertical permeability κ_z (Carcione et al., 2003),

$$\frac{\kappa_x(t)}{\kappa_z(t)} = \frac{1 - (1 - 0.3a)\sin \pi S_b}{a(1 - 0.5 \sin \pi S_b)}, \tag{14}$$

being a the permeability-anisotropy parameter.

The dry-rock bulk modulus, K_{dry}, is computed using the Krief equation (Krief et al., 1990) as follows:

$$K_{dry}(t) = K_{solid}(1 - \phi(t))^{A/(1-\phi(t))}, \tag{15}$$

where A is a dimensionless parameter which depends on the pore shape and Poisson ratio of the matrix. This parameter is a pore compliance coefficient and takes a value of about 2 for spherical pores. Assuming a relation $K_{dry}/G_{dry} = K_{solid}/G_{solid}$, we obtain the dry-rock shear modulus G_{dry} as

$$G_{dry}(t) = G_{solid}(1 - \phi(t))^{A/(1-\phi(t))}, \tag{16}$$

where G_{solid} is the solid shear modulus. Using the moduli K_{solid}, K_{dry}, G_{dry}, the porosity ϕ and permeabilities κ_x, κ_z, as well as the fluids bulk moduli and viscosities (computed using the Peng-Robinson model (Peng and Robinson, 1976) for CO_2), we determine the complex and frequency (ω) dependent Lamé coefficients $\lambda_G(\omega)$, $G(\omega)$ as

follows. In the brine saturated mudstone layers, these coefficients are obtained by using a Zener model (Carcione, 2014). Outside the mudstone layers, we consider P-wave attenuation due to wave induced fluid flow at mesoscopic scale using a model of porous layers alternately saturated with brine and CO_2 (White et al., 1975). This approach yields a complex and frequency dependent P-wave modulus $E(\omega) = \lambda_G(\omega) + 2G(\omega)$ for the formation. S-wave attenuation is also taken into account by making the shear modulus $G(\omega)$ complex and frequency dependent using another relaxation mechanism related to the P-wave mechanism (Picotti et al., 2012).

Both, Zener and White models, require the knowledge of the bulk modulus K_{solid} and density ρ_{solid} of the grains, the bulk and shear modulus K_{dry} and G_{dry} as well as the porosity ϕ and permeabilities κ_x, κ_z of the matrix. They also need the fluid bulk modulus and viscosity.

The phase velocities $v(\omega)$ and quality factors $Q(\omega)$ are defined by the relations:

$$v_t(\omega) = \left[\text{Re} \left(\frac{1}{v_{ct}(\omega)} \right) \right]^{-1}, \qquad Q_t(\omega) = \frac{\text{Re}(v_{ct}(\omega)^2)}{\text{Im}(v_{ct}(\omega)^2)}, \quad t = P, S, \tag{17}$$

where $v_{ct}(\omega)$ are the complex and frequency dependent compressional velocities defined as

$$v_{cP}(\omega) = \sqrt{\frac{E(\omega)}{\rho}}, \qquad v_{cS}(\omega) = \sqrt{\frac{G(\omega)}{\rho}}, \tag{18}$$

being ρ the bulk density defined as $\rho = (1 - \phi)\rho_{solid} + \phi\rho_{fluid}$, with ρ_{solid} and ρ_{fluid} the solid and fluid densities respectively, $\rho_{fluid} = S_b\rho_b + S_g\rho_g$.

(a) After 3 years of injection

(b) After 5 years of injection
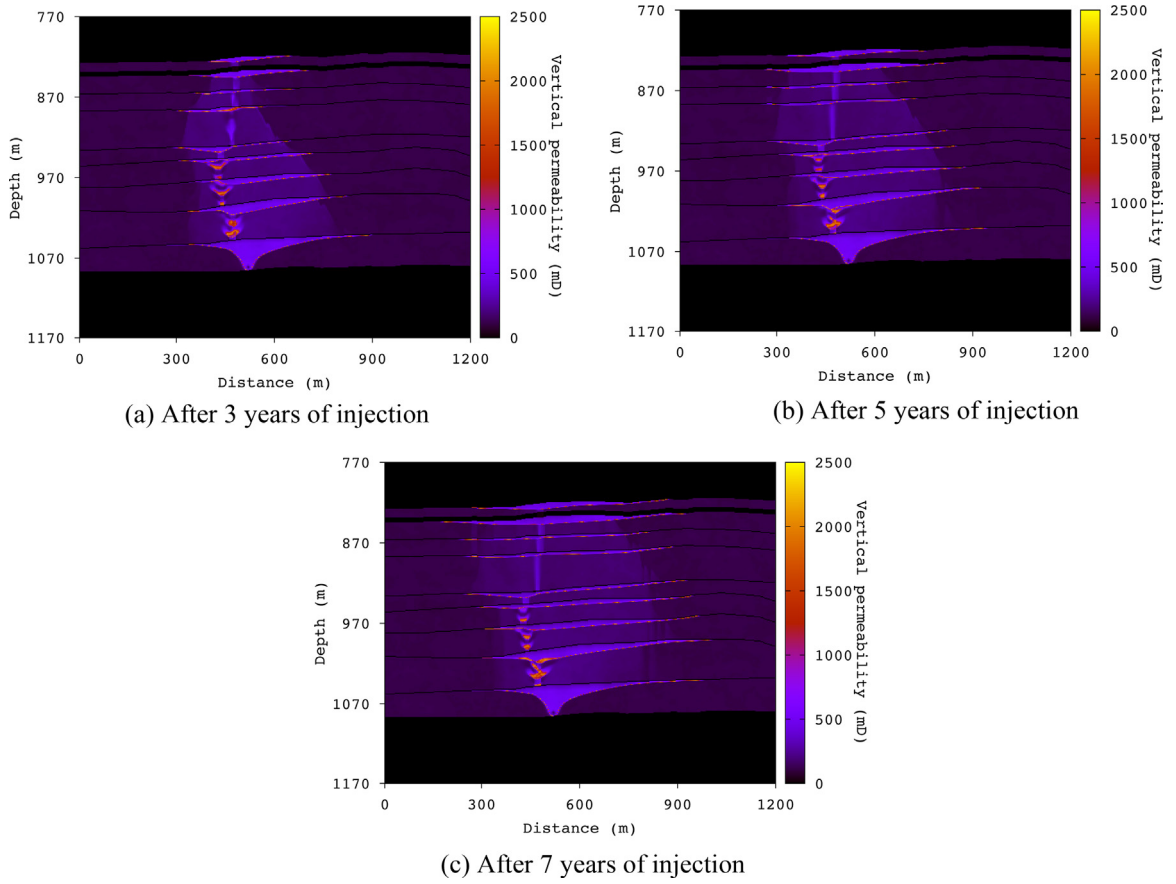

(c) After 7 years of injection

Fig. 4. Vertical permeability maps.

2.3. Wave propagation model

Wave propagation simulation is performed with our own model, which considers the effects of both wave dispersion and velocity attenuation. One of the main phenomena occurring in rocks, in particular partially saturated with CO_2, is the mesoscopic-loss effect (Carcione, 2014; White et al., 1975). This caused by heterogeneities in the fluid and solid phases greater than the pore size but much smaller than the dominant wavelengths. The mesoscopic loss causes wave attenuation and velocity dispersion of the compressional and shear waves. Since the mesoscopic scale is typically on the order of centimeters, any finite-element or finite-difference numerical procedure based on Biot's equations is impractical. To overcome this difficulty, we use an alternative approach, based on an equivalent viscoelastic medium that includes these mesoscopic-scale attenuation and dispersion effects.

The equation of motion in a 2D isotropic viscoelastic domain Ω with boundary $\Gamma = \partial\Omega$ can be stated in the space-frequency (x, ω) domain as

$$-\omega^2 \rho u - \nabla \cdot \sigma(u) = f(x, \omega), \quad \Omega \tag{19}$$

$$-\sigma(u)\nu = i\omega \mathcal{D}u, \quad \Gamma, \tag{20}$$

where $u = (u_x, u_z)$ is the displacement vector and $\sigma(u)$ is the stress tensor.

Eq. (20) is a first-order absorbing boundary condition (Ha et al., 2002), where

$$\mathcal{D} = \rho \begin{bmatrix} \nu_1 & \nu_2 \\ -\nu_2 & \nu_1 \end{bmatrix} \begin{bmatrix} \nu_{cP}(\omega) & 0 \\ 0 & \nu_{cS}(\omega) \end{bmatrix} \begin{bmatrix} \nu_1 & -\nu_2 \\ \nu_2 & \nu_1 \end{bmatrix},$$

with $\nu = (\nu_1, \nu_2)$ the unit outward normal on Γ.

The stress tensor is defined in the space-frequency domain by

$$\sigma_{jk}(u) = \lambda_G(\omega)u\delta_{jk} + 2G(\omega)\varepsilon_{jk}(u), \quad \Omega, \tag{21}$$

where $\varepsilon_{jk}(u)$ denotes the strain tensor, δ_{jk} is the Kroenecker delta, and $\lambda_G(\omega)$ and $G(\omega)$ the complex and frequency dependent Lamé coefficients defined in Section 2.2.

Appendix B describes the method used to solve the wave propagation model.

3. Numerical examples

This section presents a series of numerical examples performed with the model described in Section 2. First, we build the aquifer model based on the Utsira Sand. Then, we run the CO_2 injection simulation for several time spans to obtain the resulting CO_2 spatial distribution. Finally, we apply our wave propagation model to simulate seismic monitoring and to obtain the corresponding seismic images. We also run this series of analysis for different values of entry capillary pressure in order to evaluate its effect over the CO_2 storage procedure.

3.1. Aquifer model

We consider a 3D model of the Utsira Sand ranging 1200 m on the x-direction, 10,000 m on the y-direction, and 400 m on the vertical z-direction. The aquifer top is considered to be at a depth of 770 m (b.s.l.) (Audigane et al., 2007). The simulation is performed using a mesh with equally spaced blocks in each direction, considering 300 cells on the x-direction, 11 on the y-direction and 400 on the z-direction. Since the properties on the y-direction are constant, it is fair to say that the model is actually 2.5D.

(a) V_p map before injection

(b) V_s map before injection

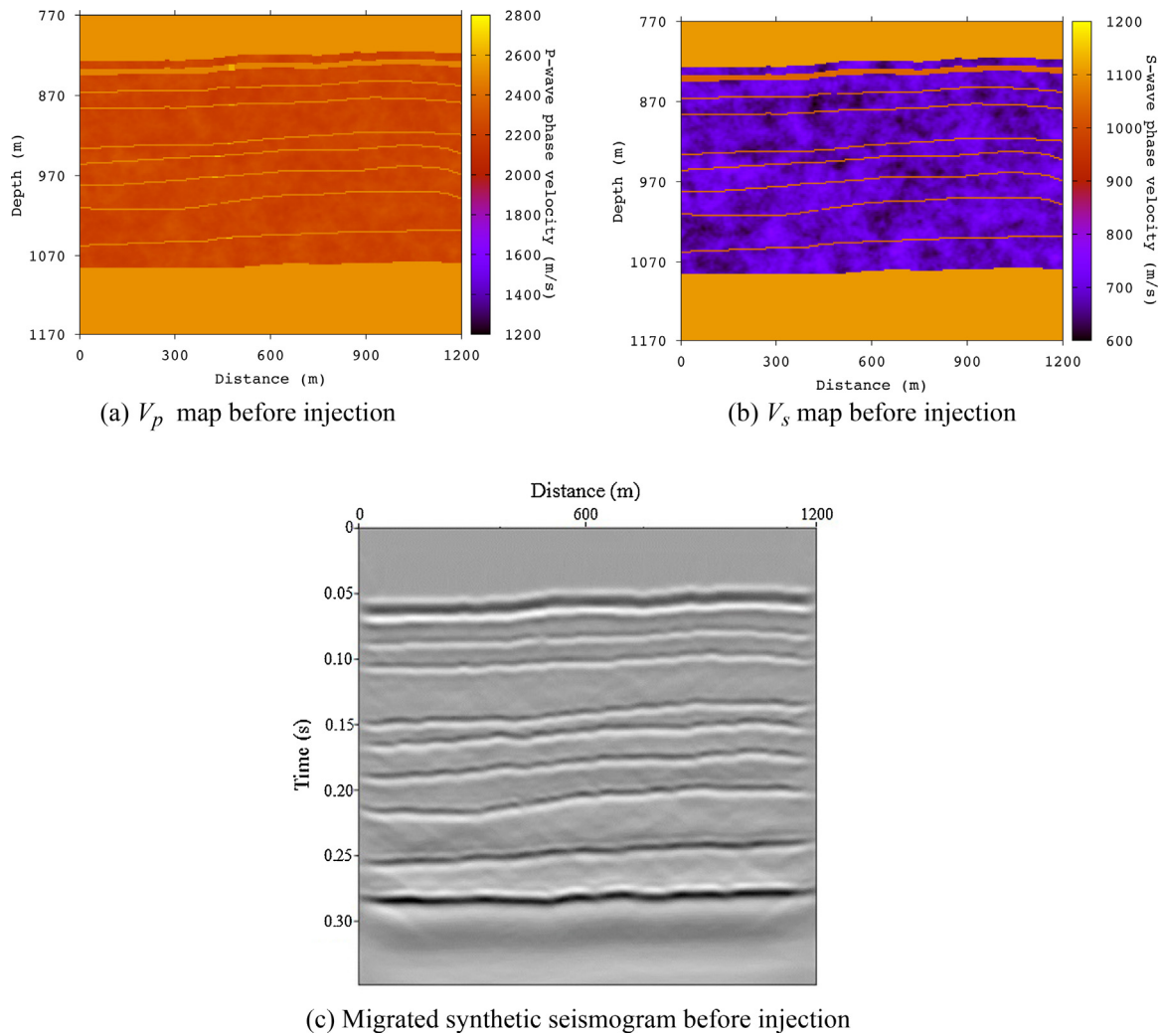(c) Migrated synthetic seismogram before injection

Fig. 5. Seismic monitoring before injection.

We consider the aquifer at hydrostatic pressure $p_H = \rho_b g z$, with $\rho_b = 1040 \, \text{kg/m}^3$ the density of brine, g the gravity constant and z the depth (in m b.s.l.). For the temperature profile we assume $T = 31.7z + 3.4$, with T in °C (Alnes et al., 2011).

The initial porosity ϕ_0 (at hydrostatic pore pressure) for the Utsira sandstone is assumed to have a fractal spatial distribution, based on the so-called von Karman self-similar correlation functions (Frankel and Clayton, 1986), using a mean value of 36.7% (Chadwick et al., 2005; Arts et al., 2008). Horizontal and vertical permeabilities are determined by using Eqs. (13) and (14), considering an anisotropy parameter $a = 0.1$ and a fixed clay content $C = 6\%$ (Carcione et al., 2006). The minimum, average and maximum initial porosities obtained are 35.5%, 36.7% and 38.3%. The associated vertical permeabilities are 0.1 D, 0.12 D and 0.145 D. The spatial vertical permeability distribution at initial conditions is shown in Fig. 1. It can be observed that, within the formation, there are several mudstone layers (low permeability and porosity) which act as barriers to the vertical motion of the CO_2. The mudstone layers topography is considered in order to represent the actual internal structure of Utsira Sand (Chadwick et al., 2004). In this regard, we have taken a picture of seismic data (Chadwick et al., 2009) and have picked the main reflections to produce a line drawing. We later have generated a geological model and produced synthetic data with plain-wave simulation. We have adjusted the model taking into account that the first internal mudstone layer is 6.5 m thick and the rest are 1 m thick (Zweigel et al., 2004). Since the model is

generated from real data, we do not claim that it is perfect, but representative of the real topography. Nevertheless, these layers are not completely sealed, having low and constant porosity and vertical permeability values of 24% and 0.033 D (Chadwick et al., 2004, 2009; Zweigel et al., 2004). Besides, each of them has an opening allowing the upward migration of CO_2. These openings are not strictly aligned, and distributed in order to help match observations from the seismic images (Chadwick et al., 2009). The overburden and underburden of the Utsira Sand are assigned constant porosity and permeability values of 32% and 0.02 D.

Fig. 2b shows the relative permeability and dimensionless capillary pressure curves that have been obtained from the conductivity log from well 15/9-13 of the Utsira Sand shown in Fig. 2a, by taking into account the relationships with the resistivity index, as described in Section 2.1.1. In particular, this capillary pressure curve has been obtained using $P_{ce} = 10 \, \text{kPa}$ based on previous studies of CO_2–brine systems (Bachu and Bennion, 2008).

3.2. CO₂ injection

We apply the BOAST simulator to model 7 years of CO_2 injection in the Utsira Sand. The simulation is performed at a constant flow rate of one million tons per year at the injection point which is located at the bottom of the formation: $x = 600 \, \text{m}$, $y = 5000 \, \text{m}$, $z = 1082 \, \text{m}$. To satisfy the CFL stability condition due to IMPES formulation (Savioli and Bidner, 2005), a constant time step of 0.08

(a) V_p map after 3 years

(b) V_s map after 3 years

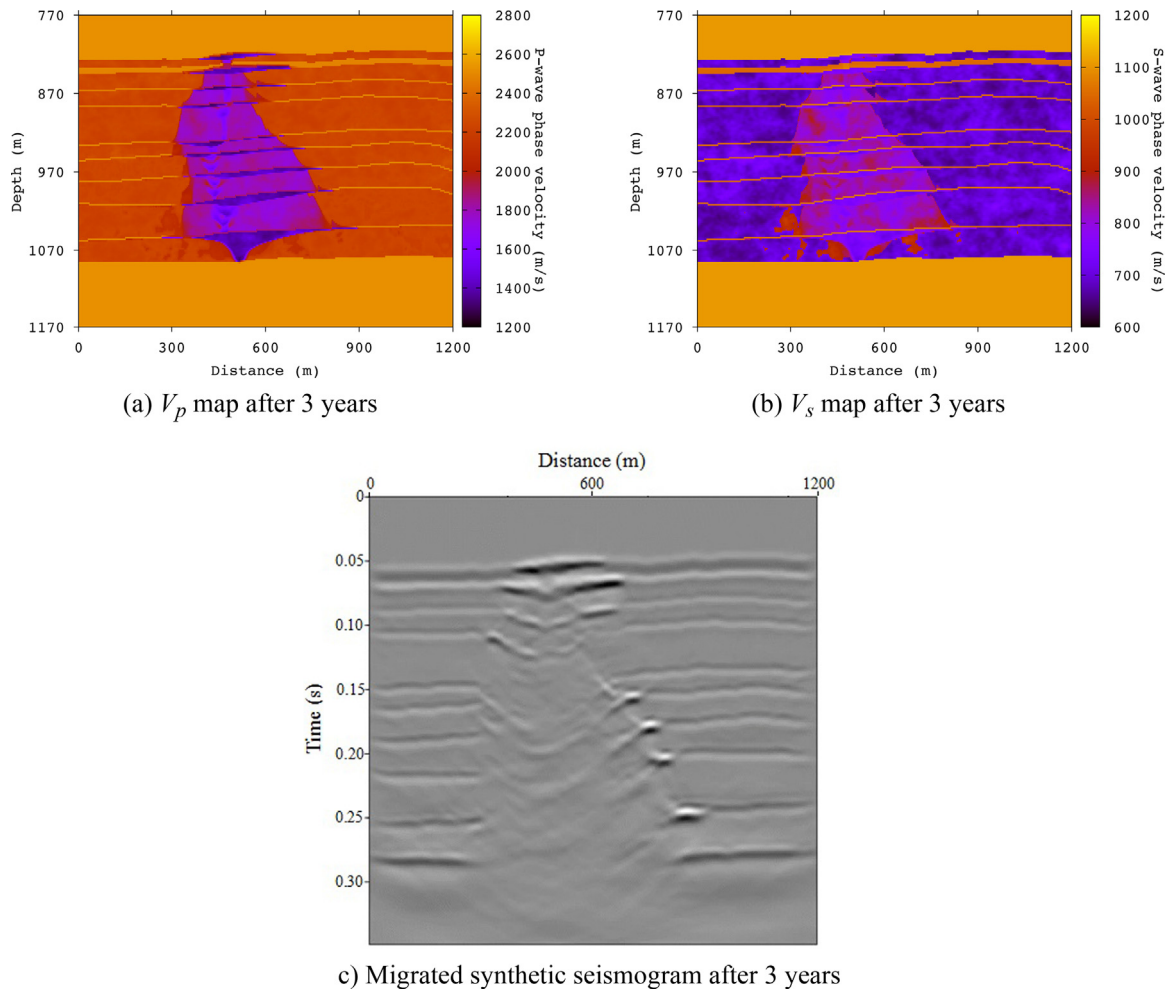c) Migrated synthetic seismogram after 3 years

Fig. 6. Seismic monitoring after 3 years of injection.

days is used. Recall that the petrophysical properties of the formation are time dependent due to the CO_2 injection and consequent increase in pore pressure, but they change at a much slower rate than pressure and saturation. As a consequence, we have two time scales, and we use a much larger time step to update petrophysical properties than to run the flow simulator. A thorough analysis has been conducted to validate that the optimum time to update the petrophysical properties would be 30 days. In this analysis, we run several simulations by gradually reducing the time step of properties update. Big differences can be observed among time steps of 1 year, 6 months and 1 month. But running the model with an update time step shorter that 30 days yield negligible differences. Therefore a time step of 30 days is considered adequate.

Fig. 3 shows the CO_2 saturation maps after 3, 5 and 7 years of injection. These maps are vertical cross sections at the injection point. CO_2 accumulations below the mudstone layers that spread laterally can be observed. As injection proceeds, the injected fluid migrates upwards through the aquifer, since its density is lower than that of the brine. Due to the presence of mudstone layers apertures, this migration generates "chimneys" because the CO_2 follows a preferred path through these openings. However, a smaller portion of it moves through the mudstone layers themselves. The openings distribution can be inferred from the shape of the chimney, which strongly depends on the position of those openings. As stated before, this distribution has been determined from seismic images (Chadwick et al., 2009). The vertical fluid flow observed is controlled by the vertical permeability. CO_2 plume reaches greater heights within the aquifer and starts to spread laterally when it reaches the top. As can be seen in Fig. 3a, after 3 years of injection the plume has already reached the top of the formation. Similar results were also achieved by other authors applying different models (Singh et al., 2010; Cavanagh and Haszeldine, 2014).

We also evaluate the behavior of the different properties that affect the fluid flow within the aquifer. Both the porosity and the horizontal permeability do not suffer significant variations, because they depend only on pore pressure (Eqs. (12) and (13)). However, the vertical permeability is assumed as saturation-dependent according to the petrophysical model (Eq. (14)), based on qualitative observations in rocks saturated with water and gas. In this model at full brine saturation, $k_x > k_z$. As water saturation is reduced, and the larger pores drained first, k_x becomes less than k_z. In fact, with CO_2 saturation around 0.5, the vertical permeability can become 1.7 times the horizontal permeability. At the other end, i.e. full CO_2 saturation, $k_x > k_z$ again. In the equations of two-phase flow in porous media (Eqs. (1) and (2)), two different permeabilities are used: the absolute permeability tensor, that contemplates the solid matrix permeabilities in each direction, and the relative permeabilities, that take into account the interactions between rock and fluids and depend only on fluid saturation. Eq. (14) allows for relative permeability anisotropy, because the relationship between vertical and horizontal absolute permeabilities is function of saturation. This is why vertical permeability, besides saturation, is the most affected property as CO_2 injection evolves, as we can see in Fig. 4.
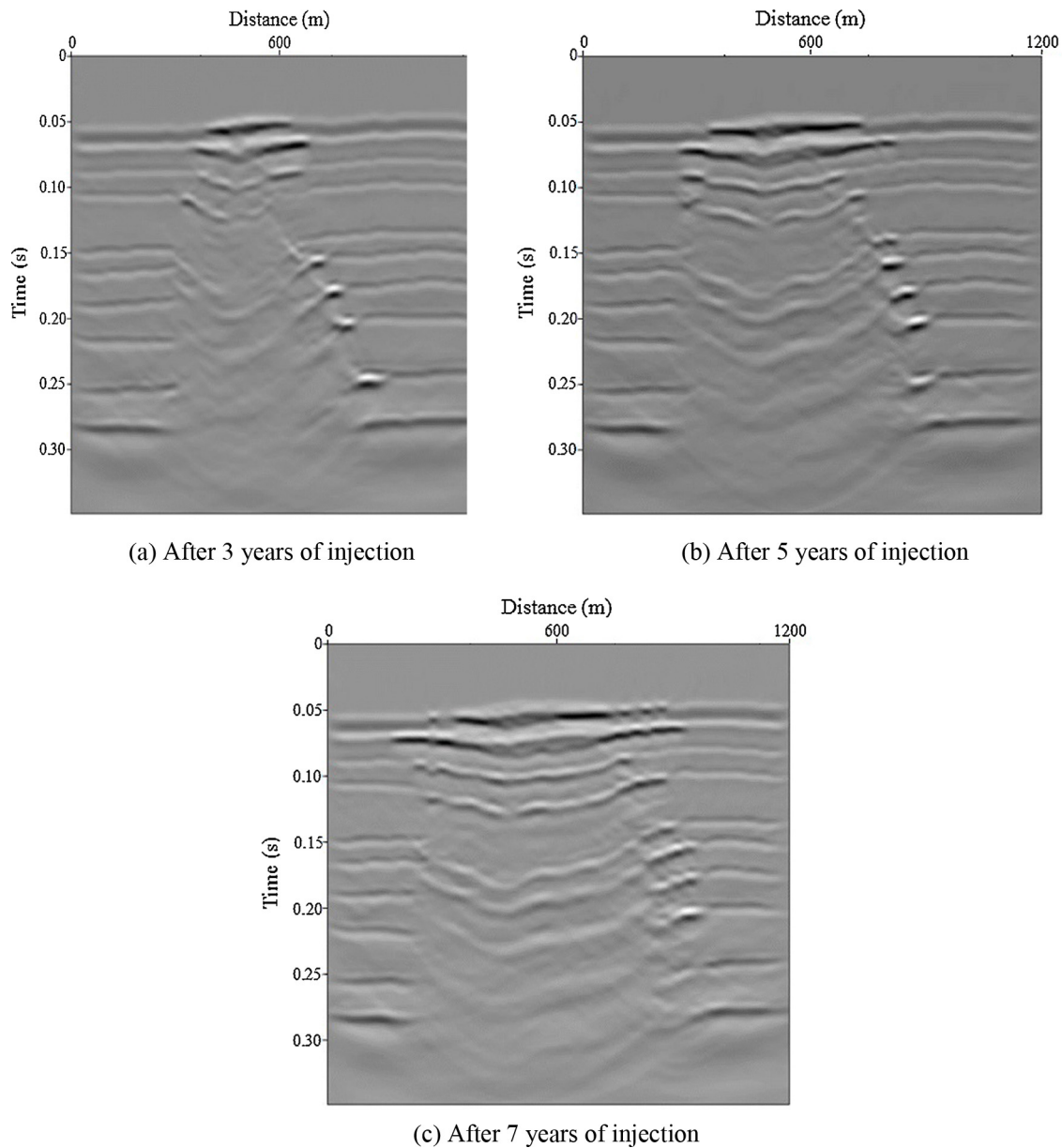
(a) After 3 years of injection

(b) After 5 years of injection

(c) After 7 years of injection

Fig. 7. Time evolution of migrated synthetic seismograms.

3.3. Seismic monitoring

In this section, we analyze the capability of seismic monitoring to identify zones of CO_2 accumulation and migration. With this purpose, saturation and pressure maps obtained by the fluid model and the corresponding updated rock properties (as described in Section 2.2) are used as input data to compute synthetic seismograms. The iterative procedure described in Eqs. (B.1) and (B.2) (Appendix B) is used to compute the time Fourier transforms of the displacement vector for 200 equally spaced temporal frequencies in the interval (0, 200) Hz. The seismic source used is a spatially localized plane wave of dominant frequency 60 Hz at $z = 772$ m. A line of receivers is located at the same depth to record the Fourier transforms of the vertical displacements. Then, a discrete inverse Fourier transform is performed to compute the synthetic seismograms (Ha et al., 2002).

Fig. 5 displays the spatial distribution of the P- and S-wave phase velocities (v_p and v_S maps) and the corresponding migrated synthetic seismogram before injection, where the mudstone layers are clearly identified. On the other hand, Fig. 6 shows the v_p map, v_S map and the migrated seismogram associated with the CO_2 saturation distribution obtained after 3 years of injection (Fig. 3a). The reduction in the P-wave velocities due to CO_2 accumulation is clearly observed.

The waves generated by the source are reflected and transmitted due to the CO_2 accumulations. The reflected waves suffer a delay when traveling in zones of CO_2 accumulation between mudstone layers. Therefore the reflections observed in the seismograms show the CO_2 distribution and accumulation.

Fig. 7 presents a comparison between the seismograms obtained after 3, 5 and 7 years of simulation. It is also clear that for different simulation times we get distinct saturation distributions (3), which result in different seismograms. As CO_2 injection develops, it spreads both laterally and vertically. Even though the absolute horizontal permeability is in general greater than the vertical one, the difference in densities for the brine and CO_2 gives the latter a much greater upward mobility. Seismic analysis can clearly detect the evolution of the CO_2 plume along time.

(a) Migrated synthetic seismogram after 5 years

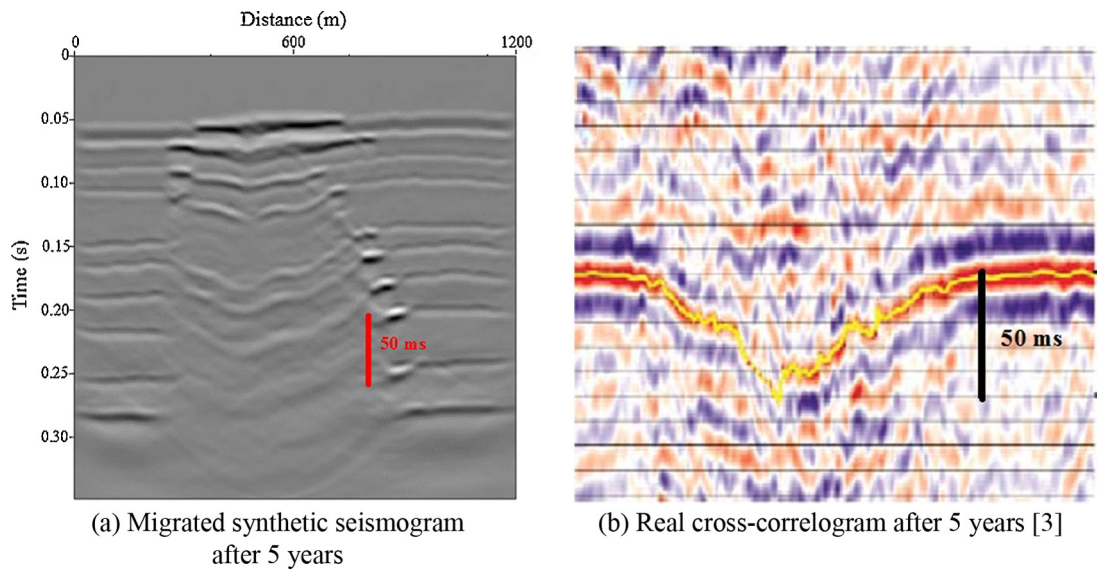(b) Real cross-correlogram after 5 years [3]

Fig. 8. Comparison between numerical results and Utsira actual data.

Finally, Fig. 8 compares the migrated synthetic seismogram obtained after 5 years of injection (Fig. 8a) with a real seismic image (Fig. 8b) obtained from Chadwick et al. (2005). It can be observed that the pushdown effect that appears in real seismograms due to CO_2 accumulations is also observed on the synthetic one. Also, the delay between the real and synthetic one is comparable. This allows us to conclude that it is possible to correlate the real saturation distribution and that obtained through the injection model.
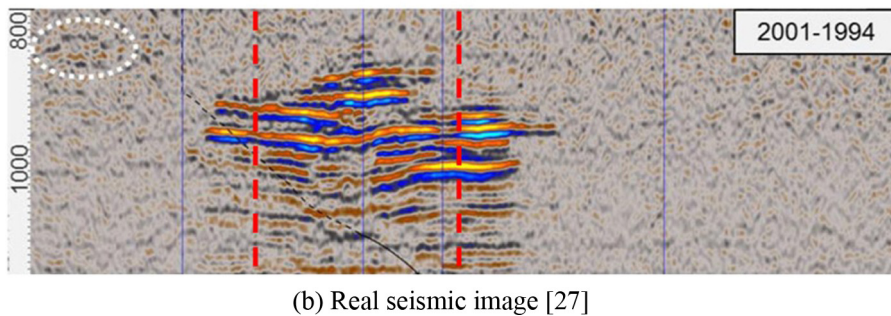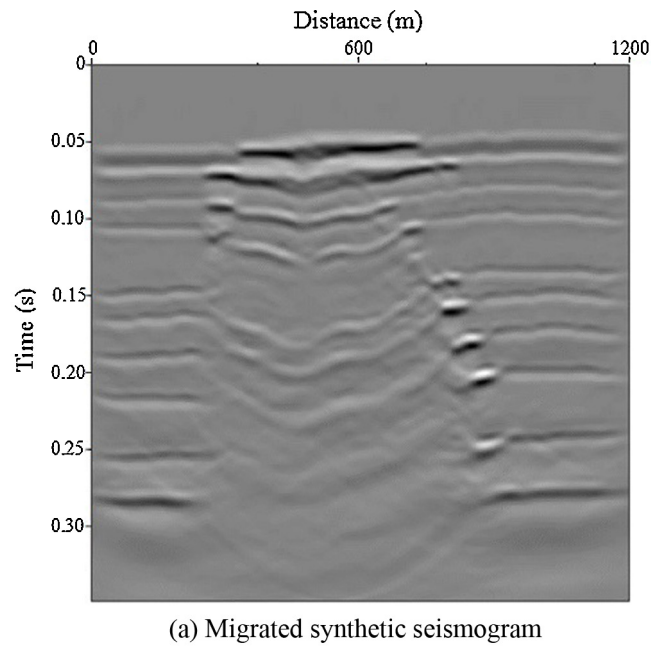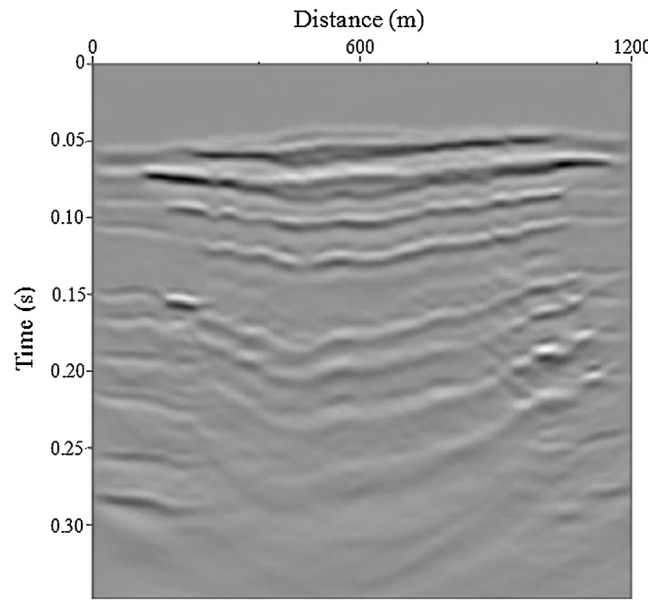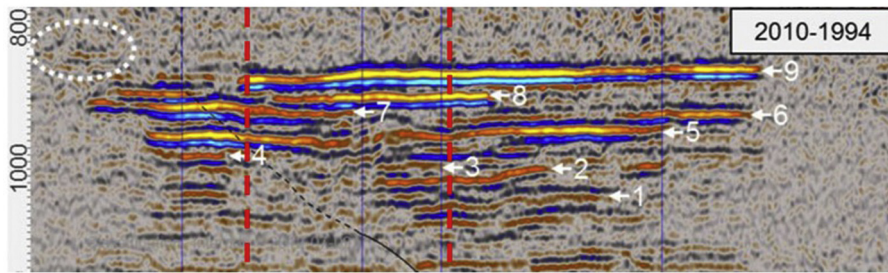

(a) Migrated synthetic seismogram

(b) Real seismic image [27]

Fig. 9. Comparison between numerical results and Utsira actual data after 5 years of injection (Furre and Eiken, 2014).

(a) Migrated synthetic seismogram

(b) Actual time-lapse seismic image [27]

Fig. 10. Comparison between numerical results and Utsira actual data after 14 years of injection.

Although the saturation map around the chimney section allows to accurately reproduce the pushdown effect, it is also observable in Figs. 9 and 10 that the lateral spread does not match the actual seismic images exactly. This is likely due to the discretization size in the *y*-direction, which has been selected to control the computational cost. Recall that the main objective of this work is not to study the plume behavior in 3D.

3.4. Capillary pressure sensitivity analysis

The results shown in previous sections consider an unique capillary pressure curve, characterized by an entry capillary pressure value of P_{ce} = 10 kPa. In this section, a sensitivity analysis is conducted for this parameter to determine its influence over the CO_2 plume evolution and the corresponding seismograms.

Several entry capillary pressure values are considered, ranging from 0.01 kPa to 200 kPa. To evaluate the plume evolution, we analyze the maximum height that CO_2 reaches within the aquifer. In order to do this, we keep track of the maximum plume length through all the time steps. This is easily computed by sweeping all the horizontal *x*-cells for every height *z* and checking whether the CO_2 saturation is higher than 0.01 (indicating CO_2 presence). This progression is shown in Fig. 11 for entry capillary pressure values of 10, 50, 100 and 200 kPa. Simulated cases with P_{ce} values lower than 10 kPa show slightly differences with the P_{ce} = 10 kPa case. It can be observed that, as capillary pressure increases, the plume upward migration velocity decreases. This CO_2 plume velocity decrease is

clearly demonstrated by the reduction of the slopes of the different curves in Fig. 11 as higher values of entry capillary pressure are used.

We also seek to evaluate the capability of the seismic analysis to identify the capillary pressure effect over the CO_2 distribution within the aquifer. For this matter we use the saturation maps obtained from the CO_2-brine flow model after 3 years of injection
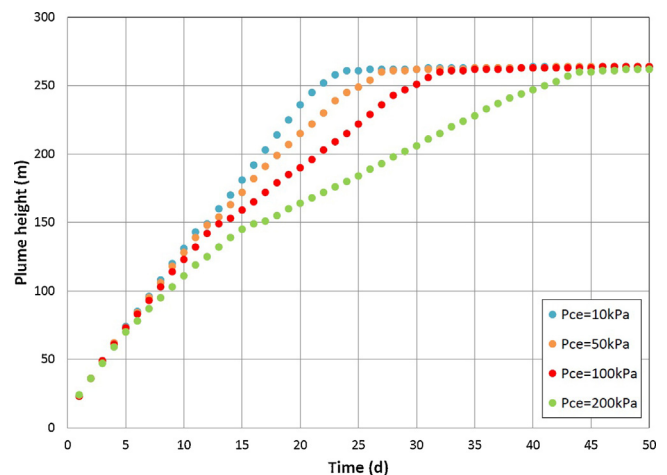

Fig. 11. CO_2 Plume height evolution for different entry capillary pressures.

(a) $PCe = 10$ KPa   (b) $PCe = 50$ KPa

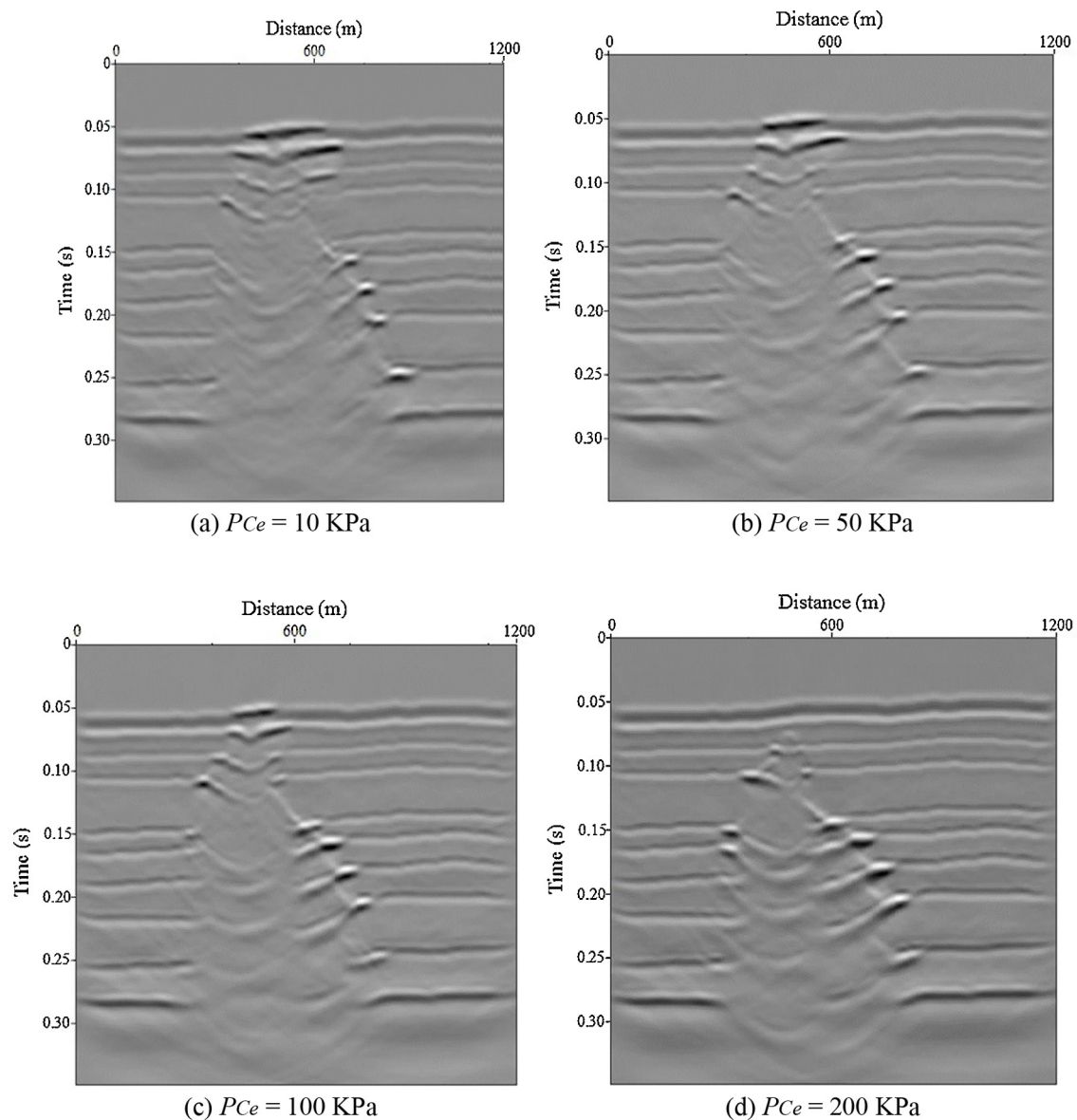(c) $PCe = 100$ KPa   (d) $PCe = 200$ KPa

Fig. 12. Entry capillary pressure effect over the migrated synthetic seismograms.

for each capillary pressure curve (e.g. Fig. 3a for $P_{ce} = 10$ kPa). With this information we obtain the seismic images shown in Fig. 12. From these images, it is clearly observed that the seismic analysis allows to identify the P_{ce} influence over the plume velocity. The presence of CO_2 is identified due to the velocity attenuation and the corresponding push down effect. As we can see in Fig. 12, the seismic images show the presence of CO_2 in different zones depending on the entry capillary pressure value. As capillary pressure increases, the plume reaches lower heights in the aquifer. That is to say, the variation of capillary pressure has a great impact on the seismic images.

4. Conclusions

We present a methodology integrating numerical simulation of CO_2-brine flow and seismic wave propagation, combined with a petrophysical model of the formation, to study and monitor CO_2 storage inside a saline aquifer. We apply this methodology to analyze the influence of capillary pressure during this process.

The flow simulator considers the CO_2 solubility in brine through a simplified thermodynamic model, with CO_2 properties determined by the Peng–Robinson equations. The petrophysical model is based on fractal porosity and considers the variation of properties with pore pressure and fluid saturation. The wave equation takes into account wave velocity changes and attenuation effects due to the presence of mesoscopic scale heterogeneities caused by patches of CO_2.

The proposed methodology has been applied to the Utsira Sand, which contains several thin low-permeability mudstone layers, which are not completely impermeable, allowing the upward migration of CO_2. The mechanism used to obtain the multiphase flow functions from well logs allows us to derive the properties that represent the fluid behavior through the Utsira Sand. The fluid-flow simulator, considering the petrophysical properties updating, yields realistic CO_2 accumulations below the mudstone layers. Besides the reflections observed in the seismograms show the progressive increase in CO_2 accumulations. In particular, the pushdown effect is clearly observed.

As can be deduced from numerical examples, capillary forces affect the migration and diffusion of the CO_2 plume; higher values of these forces cause a slower CO_2 upward migration and lateral spreading of accumulation zones below mudstone layers. Higher

entry capillary pressure values somehow slow down the advance of the CO_2 plume within the aquifer. This makes it very important to have a correct estimation of this parameter before running the simulations, because an improper value could generate wrong estimations of the CO_2 distribution within the aquifer.

Summarizing, the described methodology constitutes an important tool to monitor the migration of the CO_2 plume, to analyze storage integrity and to make long term predictions based on storage site actual data.

Acknowledgments

Appendix A. Black-Oil formulation of two phase flow in porous media

The simultaneous flow of brine and CO_2 is described by the well-known Black-Oil formulation (Aziz and Settari, 1985). In this approach, brine is identified with oil and CO_2 with gas assuming supercritical properties. Therefore, the CO_2 component may dissolve in the brine phase but the brine is not allowed to vaporize into the CO_2 phase. The Black-Oil formulation uses, as a simplified thermodynamic model, the PVT data defined as

- R_s: CO_2 solubility in brine
- B_g: CO_2 formation volume factor
- B_b: brine formation volume factor

The conversion of compositional data from equations of state into the Black-Oil PVT data is based on an algorithm developed by Hassanzadeh et al. (2008),

- $R_s = \frac{\tilde{\rho}_b^{SC} \chi_g}{\tilde{\rho}_g^{SC}(1-\chi_g)}$
- $B_b = \frac{\rho_b^{SC}}{\rho_b(1-\omega_g)}$,

where $\tilde{\rho}_b^{SC}$ and $\tilde{\rho}_g^{SC}$ are the brine and CO_2 molar densities at standard conditions, respectively and χ_g and ω_g are the CO_2 mole and mass fraction in the brine phase.

Then, the mass conservation equation for each component can be expressed as

$$-\nabla \cdot \left(\frac{1}{B_g} \underline{v}_g + \frac{R_s}{B_b} \underline{v}_b \right) + q_g$$
$$= \frac{\partial \left[\phi \left(\frac{S_g}{B_g} + \frac{R_s S_b}{B_b} \right) \right]}{\partial t} \quad \text{for } CO_2 \text{ component}, \tag{A.1}$$

$$-\nabla \cdot \left(\frac{1}{B_b} \underline{v}_b \right) + q_b = \frac{\partial \left[\phi \frac{S_b}{B_b} \right]}{\partial t} \quad \text{for brine component}, \tag{A.2}$$

where g, b denote CO_2 and brine phases respectively, ϕ is the porosity, $\underline{v}_\beta$ the phase velocity, S_β the saturation and q_β the injection mass rate per unit volume, with $\beta = b, g$.

The phase velocities can be expressed by Darcy's empirical law as

$$\underline{v}_g = -\underline{\kappa} \frac{k_{rg}}{\eta_g} (\nabla p_g - \rho_g g \nabla z), \tag{A.3}$$

$$\underline{v}_b = -\underline{\kappa} \frac{k_{rb}}{\eta_b} (\nabla p_b - \rho_b g \nabla z), \tag{A.4}$$

where p_β are the fluid pressures, η_β the viscosity, $k_{r\beta}$ the relative permeability, $\underline{\kappa}$ the absolute permeability tensor, g the gravity constant and z the depth.

Finally, combining the mass conservation equations (Eq. (A.1)) and Eq. (A.2) with Darcy's law (Eq. (A.3)) and Eq. (A.4) we obtain the following two differential equations:

$$\nabla \cdot \left(\underline{\kappa} \left(\frac{k_{rg}}{B_g \eta_g} (\nabla p_g - \rho_g g \nabla z) + \frac{R_s k_{rb}}{B_b \eta_b} (\nabla p_b - \rho_b g \nabla z) \right) \right) + \frac{q_g}{\rho_g^{SC}}$$
$$= \frac{\partial \left[\phi \left(\frac{S_g}{B_g} + \frac{R_s S_b}{B_b} \right) \right]}{\partial t}, \tag{A.5}$$

$$\nabla \cdot \left(\underline{\kappa} \frac{k_{rb}}{B_b \eta_b} (\nabla p_b - \rho_b g \nabla z) \right) + \frac{q_b}{\rho_b^{SC}} = \frac{\partial \left[\phi \frac{S_b}{B_b} \right]}{\partial t}, \tag{A.6}$$

The unknowns for the Black-Oil model are the fluid pressures p_β and saturations S_β.

Two algebraic equations relating the saturations and pressures complete the system:

$$S_b + S_g = 1, \qquad p_g - p_b = P_C(S_b), \tag{A.7}$$

where $P_C(S_b)$ is the capillary pressure function.

The numerical solution of the system is obtained with the public-domain software BOAST (Fanchi, 1997). BOAST solves the differential equations using IMPES (IMplicit Pressure Explicit Saturation), a finite-difference technique (Aziz and Settari, 1985). Finite differences is the standard in commercial reservoir simulators, and the improved versions use both structured and unstructured grids with local refinements to accurately represent reservoir geometry. The basic idea of IMPES is to obtain a single pressure equation by a combination of the flow equations. Once pressure is implicitly computed, saturation is updated explicitly. We briefly describe IMPES for these particular system (Eqs. (A.5)–(A.7)). The first step is to obtain the pressure equation, combining flow equations: Eq. (A.5) multiplied by B_g and Eq. (A.6) multiplied by $(B_b - R_s B_g)$ are added. In this way, the right side of the resulting equation is:

$$B_g \frac{\partial \left[\phi \left(\frac{S_g}{B_g} + \frac{R_s S_b}{B_b} \right) \right]}{\partial t} + (B_b - R_s B_g) \frac{\partial \left[\phi \frac{S_b}{B_b} \right]}{\partial t}.$$

Using the chain rule to expand the time derivatives and after some computations and rearrangements,

$$\phi \left[\frac{1}{\phi} \frac{d\phi}{dp_b} + S_g \left(-\frac{1}{B_g} \frac{dB_g}{dp_b} \right) + S_b \left(-\frac{1}{B_b} \frac{dB_b}{dp_b} + \frac{B_g}{B_b} \frac{dR_s}{dp_b} \right) \right] \frac{\partial p_b}{\partial t},$$

where all the time derivatives with respect to the saturation disappear.

Defining the following,

- Formation compressibility: $c_f = \frac{1}{\phi} \frac{d\phi}{dp_b}$
- CO_2 compressibility: $c_g = -\frac{1}{B_g} \frac{dB_g}{dp_b}$,
- Brine compressibility: $c_b = -\frac{1}{B_b} \frac{dB_b}{dp_b} + \frac{B_g}{B_b} \frac{dR_s}{dp_b}$,
- Total compressibility: $c_t = c_f + S_g c_g + S_b c_b$,

the right side of the resulting pressure equation is simply expressed as,

$$\phi c_t \frac{\partial p_b}{\partial t}.$$

Finally, replacing p_g by $p_b + P_C(S_b)$ in the left side of the combined equation, the following pressure equation in p_b is obtained,

$$B_g \left[\nabla \cdot \left(\underline{\kappa} \left(\frac{k_{rg}}{B_g \eta_g}(\nabla p_b - \rho_g g \nabla D) + \frac{R_s k_{rb}}{B_b \eta_b}(\nabla p_b - \rho_b g \nabla D) + \frac{k_{rg}}{B_g \eta_g} \nabla P_C \right) \right) \right]$$

$$+ (B_b - R_s B_g) \left[\nabla \cdot \left(\underline{\kappa} \frac{k_{rb}}{B_b \eta_b}(\nabla p_b - \rho_b g \nabla D) \right) \right] + B_g \frac{q_g}{\rho_g^{SC}}$$

$$+ (B_b - R_s B_g) \frac{q_b}{\rho_b^{SC}} = \phi c_t \frac{\partial p_b}{\partial t}. \tag{A.8}$$

In the BOAST simulator, Eqs. (A.6) and (A.8) are discretized using a block centered grid. The system is linearized by evaluating the pressure and saturation dependent functions (PVT parameters, viscosities, relative permeabilities and capillary pressure) in the pressure and saturation values of the previous time step. The pressure equation is solved implicitly, applying a Block Successive Over Relaxation method (BSOR) to compute the linear system solution. The saturation equation is solved explicitly, therefore stability restrictions are considered to select the time step (Savioli and Bidner, 2005).

Appendix B. The iterative domain decomposition algorithm

In order to solve the differential system (Eqs. (19) and (20)) we apply an iterative finite-element domain decomposition procedure, formulated in the space-frequency domain. To define a global finite-element method we use the nonconforming finite-element space described below, based on rectangular elements first presented in Douglas et al. (1999). For $h > 0$, let $\mathcal{T}_h$ be a quasiregular partition of $\bar{\Omega}$ such that $\bar{\Omega} = \cup_{j=1}^{J} \bar{\Omega}_j$ with Ω_j being rectangles of diameter bounded by h. Set $\Gamma_j = \partial \Omega \cap \partial \Omega_j$ and $\Gamma_{jk} = \Gamma_{kj} = \partial \Omega_j \cap \partial \Omega_k$, we denote by ξ_j and ξ_{jk} the centroids of Γ_j and Γ_{jk}, respectively.

We consider a nonconforming finite element space constructed using the following reference rectangular element:

$$\widehat{R} = [-1, 1]^2 \qquad S_2(\widehat{R}) = \text{Span} \left\{ \frac{1}{4} \pm \frac{1}{2}x - \frac{3}{8}\left((x^2 - \frac{5}{3}x^4) - (y^2 - \frac{5}{3}y^4) \right), \right.$$

$$\left. \frac{1}{4} \pm \frac{1}{2}y + \frac{3}{8}\left((x^2 - \frac{5}{3}x^4) - (y^2 - \frac{5}{3}y^4) \right) \right\}.$$

The four degrees of freedom associated with $S_2(\widehat{R})$ are the values at the mid points of the faces of $\widehat{R}$, i.e., the values at the nodal points $a_1 = (-1, 0)$, $a_2 = (0, -1)$, $a_3 = (1, 0)$ and $a_4 = (0, 1)$. For example the basis function $\psi_1(x, y) = \frac{1}{4} - \frac{1}{2}x - \frac{3}{8}\left((x^2 - \frac{5}{3}x^4) - (y^2 - \frac{5}{3}y^4) \right)$ is such that $\psi_1(a_1) = 1$ and $\psi_1(a_j) = 0$, $j = 2, 3, 4$.

A useful property of applying nonconforming elements for wave propagation phenomena is that it almost halves the number of points per wavelength necessary to reach a given accuracy as compared with the standard bilinear elements (Zyserman et al., 2003).

Set $NC_j^h = S_2(\Omega_j)$ and define a nonconforming finite-element space in the following manner:

$$NC^h = \left\{ v \mid v_j := v|_{\Omega_j} \in NC_j^h, j = 1, \dots, J; \quad v_j(\xi_{jk}) = v_k(\xi_{jk}), \quad \forall \{j, k\} \right\}.$$

The global nonconforming Galerkin procedure is defined as follows: find $\widehat{u}^h \in [NC^h]^2$ such that

$$-(\rho \omega^2 \widehat{u}^h, \varphi) + \sum_{pq} (\sigma_{pq}(\widehat{u}^h), \varepsilon_{pq}(\varphi)) + i\omega \langle \langle \mathcal{D}\widehat{u}^h, \varphi \rangle \rangle_\Gamma$$

$$= (\widehat{f}, \varphi), \quad \varphi \in [NC^h]^2,$$

Here $(f, g) = \int_\Omega f\bar{g} \, d\Omega$ and $\langle f, \bar{g} \rangle = \int_\Gamma f\bar{g} \, d\Gamma$ denote the complex $[L^2(\Omega)]^N$ and $[L^2(\Gamma)]^N$ inner products. Also, $\langle \langle \cdot, \cdot \rangle \rangle$ denotes the approximation of $\langle \cdot, \cdot \rangle$ on the boundary faces by the midpoint quadrature rule.

Instead of solving the global problem, we will use the parallelizable domain decomposition iterative hybridized procedure defined in Ha et al. (2002). This approach is a requirement when dealing with large 2D (or 3D) problems.

One of the main advantages of using nonconforming elements to solve wave propagation phenomena in parallel architectures is that the amount of information exchanged among processors in a domain decomposition iterative procedure is considerable reduced as compared to the case when conforming elements are used. Besides, it is possible to obtain an estimate on the speed of convergence of the iterative domain decomposition procedure as a function of the mesh size h.

To define the iterative procedure, we introduce a set $\widetilde{\Lambda}^h$ of Lagrange multipliers λ_{jk}^h associated with the stress values $-\tau(\widehat{u}_j)\nu_{jk}(\xi_{jk})$:

$$\widetilde{\Lambda}^h = \{\lambda^h : \lambda^h|_{\Gamma_{jk}} = \lambda_{jk}^h \in [P_0(\Gamma_{jk})]^2 = [\Lambda_{jk}^h]^2\}.$$

Here $P_0(\Gamma_{jk})$ are constant functions on Γ_{jk}. Note that Λ_{jk}^h and Λ_{kj}^h are considered to be distinct.

Then, given an initial guess $\left(\widehat{u}_j^{h,0}, \lambda_{jk}^{h,0}, \lambda_{kj}^{h,0} \right) \in [NC_j^h]^2 \times [\Lambda_{jk}^h]^2 \times [\Lambda_{kj}^h]^2$, compute $\left(\widehat{u}_j^{h,n}, \lambda_{jk}^{h,n} \right) \in [NC_j^h]^2 \times [\Lambda_{jk}^h]^2$ as the solution of the equations

$$-(\rho \omega^2 \widehat{u}_j^{h,n}, \varphi)_j + \sum_{pq} (\tau_{pq}(\widehat{u}^{h,n}), \varepsilon_{pq}(\varphi))_j + i\omega \langle \langle \mathcal{D}\widehat{u}_j^{h,n}, \varphi \rangle \rangle_{\Gamma_j}$$

$$+ \sum_k \langle \langle \lambda_{jk}^{h,n}, \varphi \rangle \rangle_{\Gamma_{jk}} = (\widehat{f}, \varphi)_j, \quad \varphi \in [NC_j^h]^2, \tag{B.1}$$

$$\lambda_{jk}^{h,n} = -\lambda_{kj}^{h,n-1} + i\beta_{jk}[\widehat{u}_j^{h,n}(\xi_{jk}) - \widehat{u}_k^{h,n-1}(\xi_{jk})], \qquad \text{on } \Gamma_{jk}. \tag{B.2}$$

It can be shown that

$$[\widehat{u}^{h,n} - \widehat{u}^h]^2 \to 0 \text{ in } [L^2(\Omega)]^2 \quad \text{when} \quad n \to \infty,$$

so that in the limit the global nonconforming Galerkin approximation is obtained (Ha et al., 2002).

Appendix C. List of symbols

a: permeability-anisotropy parameter
A: dimensionless parameter
B_b: brine formation volume factor
B_g: CO_2 formation volume factor
c_b: brine compressibility
c_f: formation compressibility
c_g: CO_2 compressibility
c_t: total compressibility
C: clay content
$E(\omega)$: frequency dependent P-wave modulus
g: gravity constant
$k_{r\beta}$: β phase relative permeability
K_{dry}: dry-rock bulk modulus
K_{solid}: solid grains bulk modulus
n: fitting parameter
p: average pore pressure
p_β: β phase pressure
p_H: hydrostatic pressure
$P_C(S_b)$: capillary pressure function
P_{cD}: dimensionless capillary pressure
P_{ce}: entry capillary pressure
q_β: β phase injection mass rate per unit volume

$Q(\omega)$: quality factor
R_c: average radii of the clay grains
R_q: average radii of the sand grains
R_s: CO_2 solubility in brine
$RI(S_b)$: resistivity index
S_β: β phase saturation
Srb: residual brine saturation
T: temperature
u: displacement vector
$v(\omega)$: Darcy phase velocity
$v_{ct}(\omega)$: compressional velocity
γ: free parameter
δ_{jk}: Kroenecker delta
$\varepsilon_{jk}(u)$: strain tensor
η_β: β phase viscosity
η_f: fluid viscosity
$\underline{\kappa}$: absolute permeability
κ_x: horizontal permeability
κ_z: vertical permeability
$\lambda_G(\omega)$: frequency dependent Lamé coefficient
G_{dry}: dry-rock shear modulus
G_{solid}: solid grains shear modulus
$G(\omega)$: frequency dependent Lamé coefficient
ρ_β: β phase density
ρ_{solid}: solid density
ρ_{fluid}: fluid density
ρ: bulk density
$\sigma(1)$: conductivity at full brine saturated rock
$\sigma(S_b)$: conductivity at saturation S_b
σ_b: brine conductivity
σ_g: CO_2 conductivity
σ_q: grain conductivity
ϕ: porosity
ϕ_c: critical porosity
ϕ_0: initial porosity

References

Alnes, H., Eiken, O., Nooner, S., Sasagawa, G., Stenvold, T., Zumberge, M., 2011. Results from sleipner gravity monitoring: updated density and temperature distribution of the CO_2 plume. Energy Procedia 4, 5504–5511.

Arts, R., Chadwick, A., Eiken, O., Thibeau, S., Nooner, S., 2008. Ten years of experience of monitoring CO_2 injection in the Utsira sand at Sleipner, offshore Norway. First Break 26, 65–72.

Audigane, P., Gaus, I., Czernichowski-Lauriol, I., Pruess, K., Xu, T., 2007. Two-Dimensional reactive transport modeling of CO_2 injection in a saline aquifer at the Sleipner site, North Sea. Am. J. Sci. 307, 974–1008.

Aziz, K., Settari, A., 1985. Petroleum Reservoir Simulation. Elsevier Applied Science Publishers, Great Britain.

Bachu, S., Bennion, B., 2008. Effects of in-situ conditions on relative permeability characteristics of CO_2-brine systems. Environ. Geol. 54, 1707–1722.

Baklid, A., Korbol, R., Owren, G., 1996. Sleipner Vest CO_2 disposal, CO_2 injection into a shallow underground aquifer. SPE Annual Technical Conference and Exhibition 36600, 1–9.

Carcione, J.M., Helbig, K., Helle, H.B., 2003. Effects of pressure and saturating fluid on wave velocity and attenuation in anisotropic rocks. Int. J. Rock Mech. Mining Sci. 40, 389–403.

Carcione, J.M., Picotti, S., Gei, D., Rossi, G., 2006. Physics and seismic modeling for monitoring CO_2 storage. Pure Appl. Geophys. 163, 175–207.

Carcione, J.M., Ursin, B., Nordskag, J.I., 2007. Cross-property relations between electrical conductivity and the seismic velocity of rocks. Geophysics 72, E193–E204.

Carcione, J.M., Gei, D., Picotti, S., Michelini, A., 2012. Cross-hole electromagnetic and seismic modeling for CO_2 detection and monitoring in a saline aquifer. J. Pet. Sci. Eng. 100, 162–172.

Carcione, J.M., 2014. Wave fields in real media: wave propagation in anisotropic, anelastic, porous and electromagnetic media. In: Handbook of Geophysical Exploration, 3rd ed., revised and extended. Elsevier.

Cavanagh, A., Haszeldine, R., 2014. The Sleipner storage site: Capillary flow modeling of a layered CO_2 plume requires fractured shale barriers within the Utsira Formation. Int. J. Greenhouse Gas Control 21, 101–112.

Chadwick, A., Zweigel, P., Gregersen, U., Kirby, G., Holloway, S., Johannessen, P., 2004. Geological reservoir characterization of a CO_2 storage site: the Utsira Sand, Sleipner, northern North Sea. Energy 29, 1371–1381.

Chadwick, A., Arts, R., Eiken, O., 2005. 4D seismic quantification of a growing CO_2 plume at Sleipner, North Sea. In: Dore, A.G., Vincent, B. (Eds.), Petroleum Geology: North West Europe and Global Perspectives - Proc. 6th Petroleum Geology Conference. , pp. 1385–1399.

Chadwick, A., Noy, D., Arts, R., Eiken, O., 2009. Latest time-lapse seismic data from Sleipner yield new insights into CO_2 plume development. Energy Procedia, 2103–2110.

Douglas Jr., J., Santos, J.E., Sheen, D., Ye, X., 1999. Nonconforming Galerkin methods based on quadrilateral elements for second order elliptic problems. RAIRO Math. Modell. Numer. Anal. (M2AN) 33, 747–770.

Fanchi, J., 1997. Principles of Applied Reservoir Simulation. Gulf Professional Publishing Company, Houston, TX.

Frankel, A., Clayton, R.W., 1986. Finite difference simulation of seismic wave scattering: implications for the propagation of short period seismic waves in the crust and models of crustal heterogeneity. J. Geophys. Res. 91, 6465–6489.

Furre, A., Eiken, O., 2014. Dual sensor streamer technology used in Sleipner CO_2 injection monitoring. Geophys. Prospect. 62, 1075–1088.

Ha, T., Santos, J.E., Sheen, D., 2002. Nonconforming finite element methods for the simulation of waves in viscoelastic solids. Comput. Meth. Appl. Mech. Engrg. 191, 5647–5670.

Hassanzadeh, H., Pooladi-Darvish, M., Elsharkawy, A., Keith, D., Leonenko, Y., 2008. Predicting PVT data for CO_2-brine mixtures for black-oil simulation of CO_2 geological storage. Int. J. Greenhouse Gas Control 2, 65–77.

Krief, M., Garat, J., Stellingwerff, J., Ventre, J., 1990. A petrophysical interpretation using the velocities of P and S waves (full waveform sonic). Log Anal. 31, 355–369.

Li, K., 2011. Interrelationship between resistivity index, capillary pressure and relative permeability. Trans. Porous Media 88 (3), 385–398.

Peng, D., Robinson, K., 1976. A new two-constant equation of state. Ind. Eng. Chem. Fundam. 15 (1), 59–64.

Picotti, S., Carcione, J.M., Gei, D., Rossi, G., Santos, J., 2012. Seismic modeling to monitor CO_2 geological storage - 1 the Atzbach-Schwanenstadt gas field. J. Geophys. Res. 117, 1–18.

Savioli, G., Bidner, M.S., 2005. Simulation of the oil and gas flow toward a well - a stability analysis. J. Pet. Sci. Eng. 48, 53–69.

Singh, V., Cavanagh, A., Hansen, H., Nazarian, B., Iding, M., Ringrose, P., 2010. Reservoir modeling of CO_2 plume behavior calibrated against monitoring data from Sleipner, Norway. In: SPE Annual Technical Conference and Exhibition.

White, J.E., Mikhaylova, N.G., Lyakhovitskiy, F.M., 1975. Low-frequency seismic waves in fluid-saturated layered rocks, Izvestija Academy of Siences USSR. Phys. Solid Earth 10, 654–659.

Zweigel, P., Arts, R., Lothe, A., Lindeberg, E., 2004. Reservoir Geology of the Utsira Formation at the First Industrial-scale CO_2 Storage Site (Sleipner area, North Sea). Geological Society, London, Special Publications, pp. 165–180.

Zyserman, F.I., Gauzellino, P.M., Santos, J.E., 2003. Dispersion analysis of a nonconforming finite element method for the Helmholtz and elastodynamic equations. Int. J. Numer. Meth. Eng. 58, 1381–1395.